Experimental Mechanics (2006) 46: 735–755
DOI 10.1007/s11340-006-9822-x

Identification of Elasto-Plastic Constitutive Parameters from Statically Undetermined Tests Using the Virtual Fields Method

Y. Pannier · S. Avril · R. Rotinat · F. Pierron

Received: 21 December 2005 / Accepted: 7 July 2006 / Published online: 23 November 2006

Abstract This paper presents an experimental validation of the use of the virtual fields method to identify the elasto-plastic behaviour of an iron specimen from full-field measurements with the grid method and a simple heterogeneous test configuration. The experimental procedure is carefully detailed since it is of primary importance to obtain good identification results. In particular, the use of two back-to-back cameras has proved essential to eliminate out-of-plane effects. Then, the procedure for extracting the elastic parameters and the parameters of a Voce's hardening model using the virtual fields method is presented. The results are very convincing and encouraging for future developments using more complex test geometries leading to fully multi-axial stress states. It is a first step towards the development of such inverse procedures as an alternative to difficult and costly methods involving homogeneous tests using multi-axial testing machines.

Y. Pannier · S. Avril (SEM member) ·
R. Rotinat (✉, SEM member) · F. Pierron (SEM member)
Laboratoire de Mécanique et Procédés de Fabrication
(JE 2381), Ecole Nationale Supérieure d'Arts et Métiers,
Rue Saint-Dominique, BP 508, 51006
Châlons-en-Champagne Cedex, France
e-mail: rene.rotinat@chalons.ensam.fr

Y. Pannier
e-mail: yannick.pannier@chalons.ensam.fr

S. Avril
e-mail: stephane.avril@chalons.ensam.fr

F. Pierron
e-mail: fabrice.pierron@chalons.ensam.fr

Keywords Optical full-filled measurements · Grid method · Identification · Elastoplastic behavior · Virtual fields method

Introduction

The experimental identification of the parameters governing the elasto-plastic constitutive behaviour of materials is a key issue which usually relies on performing simple mechanical tests for which a closed-form solution for the corresponding equivalent mechanical problem is available. These tests, such as tension or compression on prismatic specimens or torsion on thin tubes, usually lead to uniform states of stress and strain and therefore, the identification can be performed from a few strain data obtained through strain gauges or extensometers. However, in order to fully characterize the material behaviour, multiaxial tests are often necessary, requiring costly testing machines and difficult specimen design to obtain uniform stress states in some area of the specimen. Moreover, the models describing the elasto-plastic or viscoplastic behaviour of materials are governed by several parameters which cannot be directly determined from these experiments in all cases. They are in fact often identified implicitly from sets of data obtained through different experiments. Suitable identification strategies must therefore be developed to perform efficient identification. These strategies are often based on the minimization of a cost function built up with the squared difference between some measured displacement or strain components and their numerical counterparts [1–5].

An alternative to the above strategy is to perform tests leading to non uniform stress states, with the idea of retrieving more parameters from one test. Several elasto-plasticity implementations to identify material behaviour using tension and compression bending tests, along these lines, exist in the literature [6–9]. Pushing the above idea forward, some authors have proposed to retrieve elasto-plastic constitutive parameters from in-plane tests on more complex geometries either from a limited number of measurements ([10] for instance) or from a large amount of data provided for instance by an optical full-field measurement technique. In these latter cases, the identification strategies rely on finite element model updating [11–17] and most of the time, the experimental implementations presented are mainly based on the use of digital image correlation [12–14, 16, 17]. The idea is to construct a finite element model of the test to be performed using initial input values for the parameters to be retrieved. Then, the experimental data (displacements, strains and/or forces) are compared to the computed ones through a cost function to be minimized. Obviously, issues concerning existence and uniqueness of the solution are of primary importance here and depend greatly on the choice of the test, the amount of measured data and the quality of the cost function, as discussed for instance by [18]. It is interesting to note the application of this procedure to the microscopic scale to identify the local behaviour of a single crystal [16].

The Virtual Fields Method is an alternative tool that has been developed since the end of the eighties to retrieve materials mechanical parameters from full-field measurements. The first applications have focused on anisotropic elasticity ([19–21], for instance). In this case, it was shown that the virtual fields method could solve the inverse problem in a direct way. Recent progress in the choice of the virtual fields has led to the definition of "special" virtual fields [22, 23], with optimization of the virtual fields with respect to noise in the data [24]. More recently, extension of the virtual fields method was proposed for the case of elasto-plastic constitutive behaviour [25] based on simulated experimental data.

This paper presents an experimental validation of the use of the Virtual Fields Method (VFM) to identify the parameters of an elasto-plastic constitutive model, namely Voce's non-linear hardening model) from a simple heterogeneous test configuration and the grid method. After a brief description of the experimental set-up, of the full-field optical measurement technique and of the identification procedure, results are presented and compared with the ones obtained with standard tests.

Experimental Procedure

Standard Material Characterization

The material studied here is 99.5% pure iron. It is in the shape of a 2 mm sheet in which the specimens have been cut. The material has been characterized by standard tension tests on prismatic coupons using six samples. All the specimen were cut in the rolling direction of one single metal sheet so as to avoid a variation of mechanical properties due to the anisotropy induced by rolling.

The transverse and longitudinal specimen directions are denoted by x and y, respectively. The longitudinal stress component σ_{yy} is the only component to be considered in the following and it is simply denoted σ.

Strains ε_{xx} and ε_{yy} have been measured from bi-directional rosettes bonded back-to-back on the specimen to account for parasitic bending effects caused by grip misalignment. The stress σ is given by the ratio between the applied load and the cross section area of the specimen.

The stress–strain curves σ vs ε_{yy} and σ vs ε_{xx} are linear before yielding. Young's modulus and Poisson's ratio are deduced from the slopes of the curves.

The stress–strain curves after yielding are non linear. The relationship between the σ stress (Von Mises stress which here reduces to σ) and the effective plastic strain $\varepsilon^p = \varepsilon_{yy} - \sigma/E$ has been fitted by Voce's non-linear hardening model [26] and is expressed as:

$$\sigma = \sigma_0 + R_0\varepsilon^p + R_{\text{inf}}\left[1 - \exp(-b\,\varepsilon^p)\right] \tag{1}$$

where σ_0 is the initial yield stress, R_0 the linear asymptotic hardening modulus, R_{inf} and b the parameters that describe the non linear part of the response in the initial yielding zone.

Therefore, six parameters have been identified: Young's modulus E, Poisson's ratio ν, and the plastic parameters σ_0, R_0, R_{inf} and b (Table 1).

Heterogeneous Mechanical Test

The idea of the present approach is to perform a test that will lead to a heterogeneous state of stress and strain in which there is no explicit relationship between the local stresses and the applied load (statically undetermined test). The objective is to retrieve all the parameters reported in Table 1 driving the stress–strain curve of the material, but this time using the VFM.

Table 1 Reference values for the material parameters identified with the standard tensile tests

	E (GPa)	ν	σ_0 (MPa)	R_0 (GPa)	R_{inf} (GPa)	b
Mean	199	0.32	127	2.46	56.2	3.37×10^3
Coeff. of var. (%)	1.3	6.2	12	20	25	21

However, since this is the first attempt at using the VFM for elasto–plastic constitutive equations with experimental data, it was thought that a mainly uniaxial stress configuration would be a good starting point. Therefore, a flat dogbone specimen has been chosen so that as a first approximation the longitudinal stress only varies longitudinally and the other stress components remain negligible. The specimen is shown in Fig. 1 together with the mechanical arrangement (grips, camera ...). The specimen has been cut in the rolling direction of the metal sheet used for the standard tests.

It has been verified using finite element analysis that the assumption of a uniaxial stress state is reasonable. The stress field has been plotted for an applied load causing stresses beyond the yield point in the whole area of interest (Fig. 2). It shows that the stress components σ_{xx} and σ_{xy} are very low compared to the longitudinal stress component σ_{yy}. Therefore, σ_{xx} and σ_{xy} will be neglected in this study. Only the longitudinal stress component σ_{yy} (denoted σ) will be considered. The objective of this assumption is to validate the approach in a relatively simple case before extending it to a fully multi-axial stress state. The virtual fields method is however perfectly able to tackle the full problem, as demonstrated in [25].

In the present situation, the longitudinal stress field σ is however heterogeneous, varying from one cross section to another and also along the cross sections (Fig. 2). Accordingly, the stress field cannot be linked explicitly to the applied load anywhere over the area of interest, meaning that the current mechanical test is indeed statically undetermined. The use of an inverse procedure is therefore necessary to identify the constitutive parameters.

Displacement Field Measurements

A variety of full-field experimental techniques exist to characterize 2D displacement fields [27]. Among those, the optical methods have the advantage to be non-contact and non-disturbing. These techniques can be sorted according to various criteria, such as the nature of the physical phenomenon involved (interferometric, non-interferometric) or the nature of information

Fig. 1. Specimen with mechanical and optical set-up

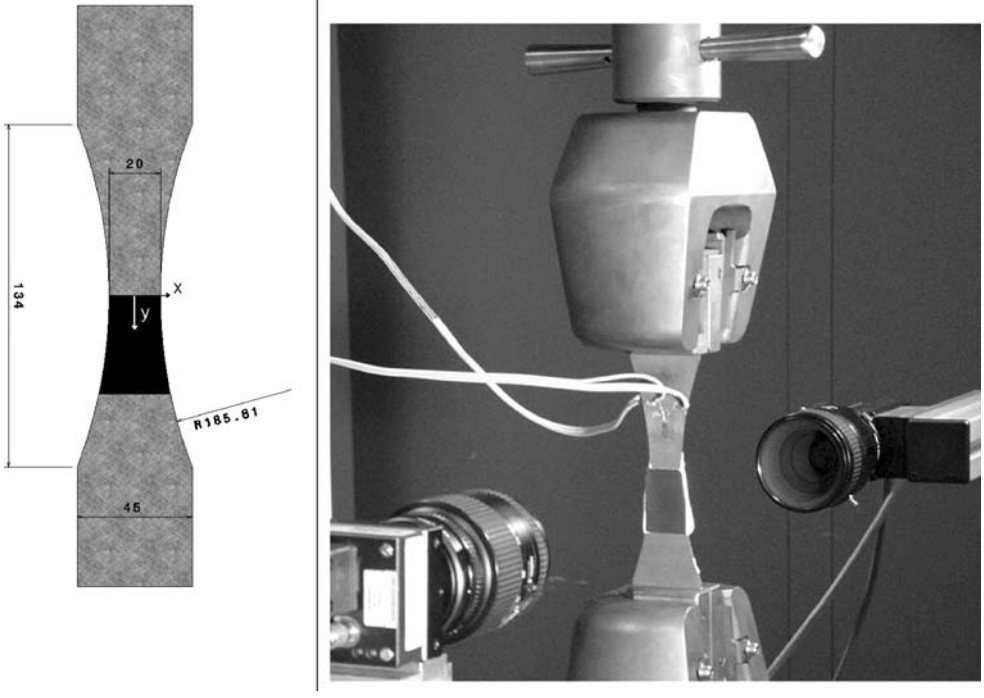

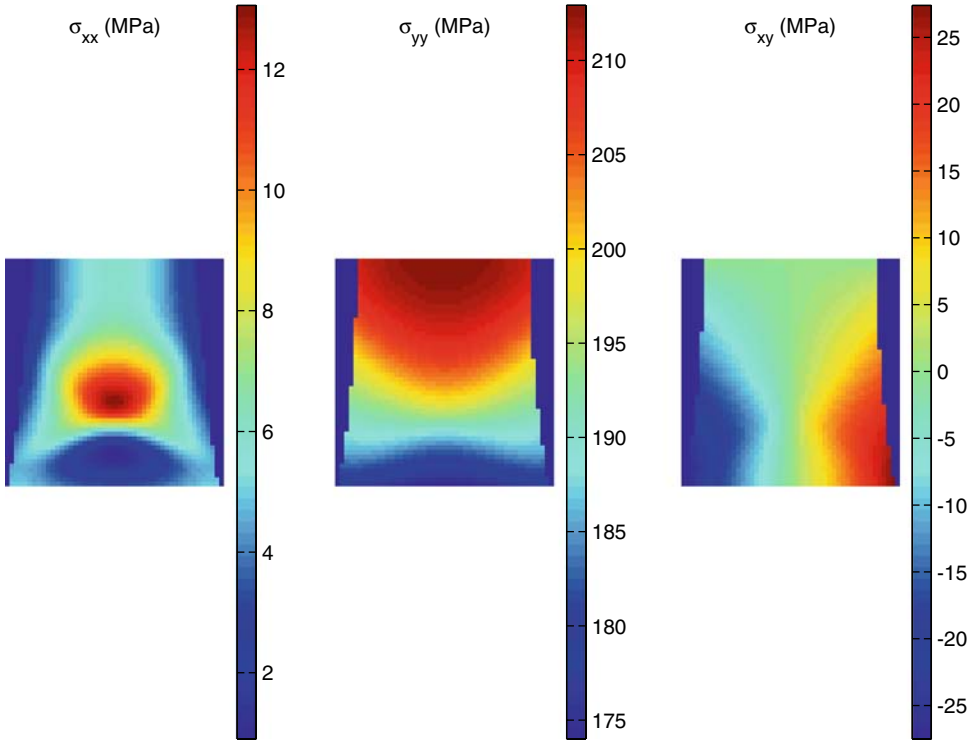

Fig. 2. Stress fields computed by FEM over the area of interest (applied load: 8,400 N ⇔ average stress of 210 MPa in the middle cross section)

encoding (random, periodical) [28]. The grid method is the full-field measurement technique chosen here. It is a non-interferometric technique that uses a periodical encoding. Let us note that non-interferometric techniques are also often called geometrical methods because optics is restricted to image information.

Principle

The grid method [29] is based on the analysis of the deformation of a carrier grid, defined by a pitch p, fixed to the plane surface to study. The grid can be unidirectional or bidirectional (cross-lines). A grid pattern of cross-lines, deposited onto the surface of the specimen (Grid bonding), makes it possible to measure the two components of the displacement field. The information characterizing the displacement field of the specimen is found in the phase modulation of a spatial (or temporal) carrier. The measurand (i.e., displacement) is related (linearly or not) to the phase.

Characterization of the phase modulation Let us consider a given point M of the space characterized by its position vector $\vec{r}(x, y)$ in the cartesian reference frame $(O, \vec{\imath}, \vec{\jmath})$. In the initial (undeformed) state, M coincides with a material point M_0 of the grid. The intensity of the light at M coming from M_0 is given by:

$$I(M) = I(M_0) = I_0\left[1 + \gamma\ \mathrm{frng}\left(2\pi\vec{f}_x \cdot \vec{r}\right)\right.$$
$$\left.\mathrm{frng}\left(2\pi\vec{f}_y \cdot \vec{r}\right)\right] \qquad (2)$$

where:

- I_0 is the average intensity or bias,
- γ is the contrast or visibility of the signal lying in the range [0;1],
- frng is a 2π-periodic continuous function,
- $\vec{f}_x$ and $\vec{f}_y$ are the spatial frequency vectors, respectively, associated to the vertical and horizontal lines. They are orthogonal to the grid lines and their amplitudes are the spatial frequency of the grid. If the grid lines are horizontal (parallel to $\vec{\imath}$) and vertical (parallel to $\vec{\jmath}$), the spatial frequency vectors write, respectively, $\vec{f}(0, f_0)$ and $\vec{f}(f_0, 0)$ with $f_0 = 1/p$.

When a load is applied, there is a deformation of the solid and the grid also deforms. In the final (deformed) state, M coincides with the material point M_1. M_1 is characterized, in the initial state, by a position vector

$\vec{r}_1(x, y)$ in the cartesian reference frame and by the intensity of the light reflected by this point, given by:

$$I(M_1) = I_0\left[1 + \gamma\ \mathrm{frng}\left(2\pi\vec{f}_x \cdot \vec{r}_1\right)\mathrm{frng}\left(2\pi\vec{f}_y \cot\vec{r}_1\right)\right] \tag{3}$$

However, the deformation from the initial state to the final state is described mathematically by the displacement field $\vec{u}(M_1) = \vec{r} - \vec{r}_1$. Therefore Eq. 3 becomes:

$$I(M) = I_0\Big\{1 + \gamma\ \mathrm{frng}\left[2\pi\vec{f}_x \cdot \left(\vec{r} - \vec{u}(M_1)\right)\right] \mathrm{frng}\left[2\pi\vec{f}_y \cdot \left(\vec{r} - \vec{u}(M_1)\right)\right]\Big\} \tag{4}$$

If the deformation is small between two images, $\vec{u}(M_1)$ and $\vec{u}(M_0)$ are equal. Therefore, it can be written in the deformed state:

$$I(M) = I_0\Big\{1 + \gamma\ \mathrm{frng}\left[2\pi\vec{f}_x \cdot \left(\vec{r} - \vec{u}(M_0)\right)\right] \mathrm{frng}\left[2\pi\vec{f}_y \cdot \left(\vec{r} - \vec{u}(M_0)\right)\right]\Big\} \tag{5}$$

This relation is the basis of the grid technique for displacement field measurement. From the initial to the final state, the phases $\phi_x = 2\pi\vec{f}_x \cdot \left[\vec{r} - \vec{u}(M_0)\right]$ and $\phi_y = 2\pi\vec{f}_y \cdot \left[\vec{r} - \vec{u}(M_0)\right]$ of the functions frng representing the light intensity acquired at point M varies of $\Delta\phi_x = -2\pi\vec{f}_x \cdot \vec{u}(M_0)$ and $\Delta\phi_y = -2\pi\vec{f}_y \cdot \vec{u}(M_0)$ for the vertical and the horizontal grid lines, respectively.

The phase map from an initial state to a final state of a specimen can only be obtained from the subtraction of two states of the grid. Therefore, two images are necessary to measure the displacement vector, since it is given by the difference between two phase patterns obtained from the initial and final states.

In experiments, the map of the intensity reflected by the grid is recorded with a CCD camera. To obtain the in-plane displacement field, it is necessary to extract the quantitative phase from the recorded intensity field. Indeed, the corresponding phase fields can be deduced from the intensity field described by Eq. 5. Different techniques exist in the literature [29–31]. The one used here is called phase shifting.

Phase Detection by phase shifting Equation 5 is the general form of a measured intensity field. There is an infinity of unknown factors. Indeed, the frng function (line profile) can be defined by an infinity of Fourier coefficients, which would have to be identified to extract the phase. The mean intensity I_0, the contrast γ and the phase are also unknown. Thus, recording only the intensity field does not make it possible to deduce the phase, since there is one equation for at least four unknown factors (if function frng is harmonic). This is why supplementary equations are needed to solve the system. These additional equations can be obtained by the method of phase shifting, which can be either spatial or temporal [29].

At every pixel of the CCD detector, a sample is recorded. The number of pixels sampling a period of the grid should be an integer denoted N. The phase fields are calculated here by using the spatial phase shifting method associated with a N-bucket algorithm. The success of this algorithm strongly depends on the sampling frequency. One period of the grid must be sampled by exactly an integer number N of pixels. In practice, this proves impossible to do it because the grid deforms after loading. Therefore, it is necessary to use a specific type of N-bucket algorithm, called Windowed Discrete Fourier Transform (W-DFT) [32, 33]. It corresponds to the computation of the discrete Fourier transform of the set of intensity samples, windowed by a triangle function. It realizes an extraction of 2N-1 images from the initial image of the grid by taking only one pixel over 2N-1 at each time. In this case, for a given set of 2N pixels, the phase is:

$$\phi = \arctan\left(-\frac{\sum_{k=1}^{N-1} k(I_{k-1} - I_{2N-k-1})\sin(2\pi k/N)}{NI_{N-1} + \sum_{k=1}^{N-1} k(I_{k-1} + I_{2N-k-1})\cos(2\pi k/N)}\right) \tag{6}$$

where I_k is the light intensity of the k^{th} pixel ($k = 0 \ldots 2N-1$) , N the number of pixel sampling a grid period, and $\delta = 2\pi/N$ the phase shift.

The algorithm is insensitive to a linear phase-step miscalibration α, such that the k^{th} phase offset introduced in the phase-shifting procedure is $\delta_k = k\delta(1+\alpha)$ [32]. Consequently, the W-DFT algorithm is considered insensitive to a linear phase-step miscalibration. Moreover, the algorithm is insensitive to harmonics up to the order of $N-2$, even in the presence of a phase-shift miscalibration.

The complete image processing including this phase determination method is presented in Fig. 3. A digital camera performs the spatial sampling and acquisition of the intensity of the grid. An algorithm enables the separation of the two directions by averaging the signal in the other direction over two periods. Ten phase-shifted

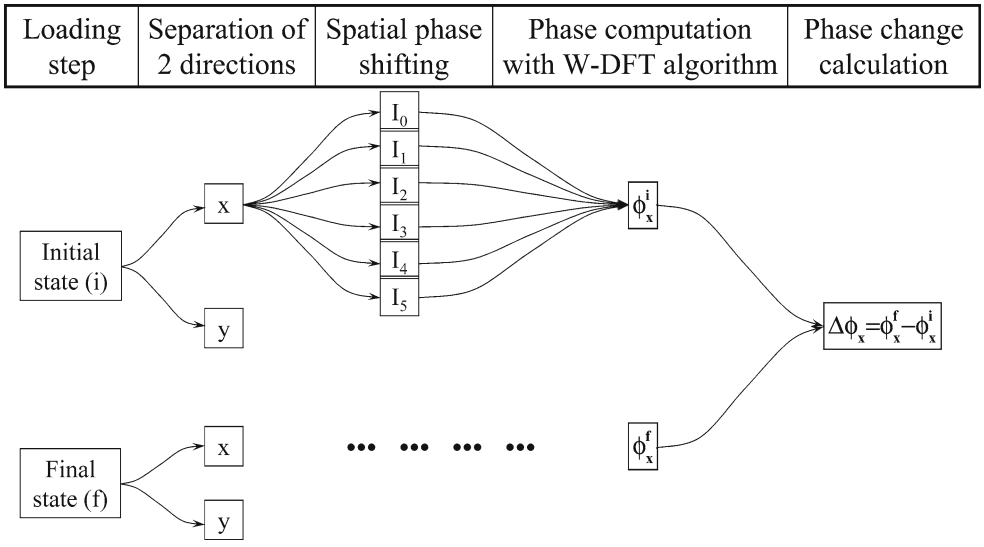

Fig. 3. Procedure to obtain phase change maps

intensity samples (N=10) are employed here for the evaluation of one phase map by spatial phase shifting. For each point, the local phase difference is related to the displacement in the direction normal to the considered lines.

Displacement field evaluation The $u_x(x, y)$ and $u_y(x, y)$ displacement fields relative to the unloaded reference condition are calculated from the respective phase differences $\Delta\phi_x$ (for vertical lines) and $\Delta\phi_y$ (for horizontal lines) introduced by the deformation:

$$u_x(x, y) = -\frac{p}{2\pi}\Delta\phi_x(x, y) \tag{7}$$

$$u_y(x, y) = -\frac{p}{2\pi}\Delta\phi_y(x, y) \tag{8}$$

where p is 0.2 mm here. The resolution of the method, i.e., the smallest displacement which can be measured in absolute value, depends on the measurement noise. The noise is often assumed to be a random variable which adds to the phase during the calculation [33]. Its mean value is zero and its standard deviation is denoted σ_ϕ. In our experiments, σ_ϕ is about $2\pi/300$ radians i.e., 1.2 degree. The resolution of the method is defined by $\sigma_u = \sigma_\phi/s$. The sensitivity of the grid technique is given by $s = 2\pi/p$. In our application, the resolution of the method for measuring displacements is approximatively 0.67 μm. The spatial resolution, which is the distance separating two independent measurement pixels, is 380 μm.

Grid bonding

Obtaining regular grids is a key issue in the success of the grid method. Several methods for physically applying grids onto a specimen surface are available in the literature. Grids can be etched, ruled, printed, stamped, photographed or cemented onto specimens [34]. The suitability of each technique mainly depends on the frequency of the grids. Many techniques exist (laser marking, lithography, micro erosion, photo-electrodeposition...) and are well developed to manufacture high frequency grids [35]. Conversely, few techniques exist for low frequency gratings (one to a few tens of lines per mm). The technique selected here makes it possible to obtain inexpensive grids with ten features per millimeter of good metrological quality. They are manufactured by printing on photosensitive films and transferred to the specimen by adhesive bonding [36].

A PostScript file containing the description of the grid is used as input to the printer. The lines of the grid must be separated by the same distance p. The variation of this distance should be as low as possible. A variation of 1% on p is responsible for a relative error of 1% in the measurement. In this file, the pitch of the grid can be adjustable. It is also possible to adjust or correct the ratio between the black and the white of the printed grids.

Usual inkjet and laser printers have a low resolution going up to about 700 dpi. To avoid this limitation, a Heidelberg Recorder 3030 plotter for graphic art, having a nominal resolution of 4, 877 dpi, was used. The pitches that can be obtained lie between 0.02 mm and 2 mm in theory. In practise, for a pitch below 0.1 mm,

the black-to-white ratio of the printed grids was not equal to the target. This fact is due to the bad response of the plotter. It is interesting to note that the black-to-white ratio can be set to a value lower than one to compensate for the bias of the plotter, at least up to a certain point. This issue will be investigated in the future but for the present study, a pitch of 0.2 mm proved sufficient.

The transparencies used for printing the grids on are photographic films, different from those suitable for usual inkjet and laser printer. They consist of a polymeric transparent backing covered with photosensitive emulsion. Since the backing is rather thick, it is not desirable to leave it at the surface of the tested specimen as it may affect its mechanical response and reduce the contrast of the grid. Therefore, it is necessary to "transfer" the grid, ie, bond the film on the specimen and peel off the backing after the glue has cured. This used to be achieved by "stripping films" but these have now disappeared from the market. Several types of photographic films have been tested. Most of them led to impossible transfer of the grids (photosensitive emulsion) because of a too high adhesion between film and glue. Eventually, the Ferrania image-setting photographic film AI PO-50 proved to be suitable for this type of use. The transparency is a permanent antistatic polyester base with an optimum dimensional stability. Its thickness is 0.1 mm and it is available in any standard size. The photographic emulsion is negative etching, sensitive to blue light (488 nm).

The glue used to transfer the photographic coating from the film to the specimen surface is marketed under the E504 denomination by the company "Épotechny". It is a white two-parts epoxy resin, enabling the optical contrast with the black lines, thus preventing the addition of a layer of paint. A study of the mechanical response of the adhesive [36] revealed a behaviour close to that of the M200 adhesive provided by Vishay Micromeasurements (adhesive for strain gauges).

The transfer process of grid consists in bonding the side of the film with the emulsion on the specimen surface. At the end of the curing process of the glue, the adhesive has a much stronger link with the emulsion than that between the emulsion and the polyester backing, which makes it possible to peel off the backing so that only the printed emulsion and the glue stay at the surface of the specimen. The details of the grid transfer method are as follows:

- Remove grease and dirt on both specimen and grid;
- Coat with a thin layer of glue both the surface of the specimen and the photographic emulsion side of the grid;
- Press slightly with a piece of gauze to expel the air bubbles and the excess glue;
- Apply a pressure of about 5 kPa during the curing of the glue;
- Cure the glue during 39 hours at 35°C,
- Peel off the film carefully and slowly.

The average thickness of the cured glue and grid is lower than 0.1 mm in all cases, which, considering the very low stiffness of the glue compared to the metal specimen, leads to negligible effects of the grid marking on the mechanical response of the test specimen.

Out-of-plane effects

The performance of optical systems is limited by several factors, including lens aberrations and distortions. But the displacements are obtained by substraction between an initial and a final state. Therefore, for small displacements between two consecutive images, the effects of the lens can be ignored, since it is the same physical area of the lens that will image the grid in the deformed and undeformed state. Therefore, the effects of possible aberrations will cancel out.

However, measurements of in-plane displacements are sensitive to out-of-plane movements of the specimen when an imaging lens is used. Indeed, the magnification depends on the imaging distance and any change of this distance induces a change of magnification that the system interprets as strains.

As a first approximation, the lens of the optical system can be represented by the simple model of a thin lens. A paraxial calculation gives a well known linear relationship between the out-of-plane movement and the parasitic induced strain denoted $\varepsilon^{\text{parasitic}}$:

$$\varepsilon^{\text{parasitic}} = \frac{\mathrm{d}z}{z} \tag{9}$$

where $\mathrm{d}z$ represents the out-of-plane displacement and z the nominal distance between the object and the camera. However, out-of-plane displacements up to 100 μm are common during a mechanical test. If, for example, z is close to 200 mm during the test, the parasitic strains thus induced amount to 5.10^{-4}. This is not acceptable considering the requirements of the experiments (strain elastic limit of about 1.10^{-3} for our material).

The use of a telecentric lens would solve this problem but other issues like lighting, cost and lack of flexibility makes this solution rather inconvenient. Indeed, this kind of lens imposes the image distance and the magnification to be fixed. Another possibility for solving this problem consists in measuring the displacements on both sides of the specimen using two cameras.

Two-camera set-up

Let us consider two strictly identical frame grabbing systems, in particular for the size of the CCD sensor and for the focal length of the photographic lens. Figure 1 shows the two-camera set-up: the two frame grabbers are placed at the same distance on each side of the specimen. Considering the tensile specimen as a beam, it can be subjected to two out-of-plane parasitic effects: rigid body movement and bending deformation.

Out-of-plane rigid body movement can be the consequence of clearance between the elements of the machine.It is represented by a u_z displacement and a R_z rotation (Fig. 4). These displacement and rotation have opposite effects between the front and the back side of the specimen. The relation 9 being linear, $\varepsilon^{\text{parasitic 1}} = -\varepsilon^{\text{parasitic 2}}$. By averaging the strain maps obtained on each face of the specimen, the out-of-plane rigid body effects are cancelled.

The other parasitic effect is that caused by an out-of-plane bending moment. This can be the consequence of misalignment of the grips or bad guiding of the crosshead of the tensile machine. This movement will create extra longitudinal stresses: tensile on one face and compressive on the other. An additional negative in-plane strain will be added up on the front face, and a positive one will be added up on the back face. Therefore, the measurement of the strain field will be biased if only one face is instrumented. The out-of-plane bending is critical at the early stage of the test, i.e., when the response is elastic linear. Indeed, when the loading increases, the specimen gets in line with the grips of the machine and the effect of bending becomes negligible. In the elastic linear state:

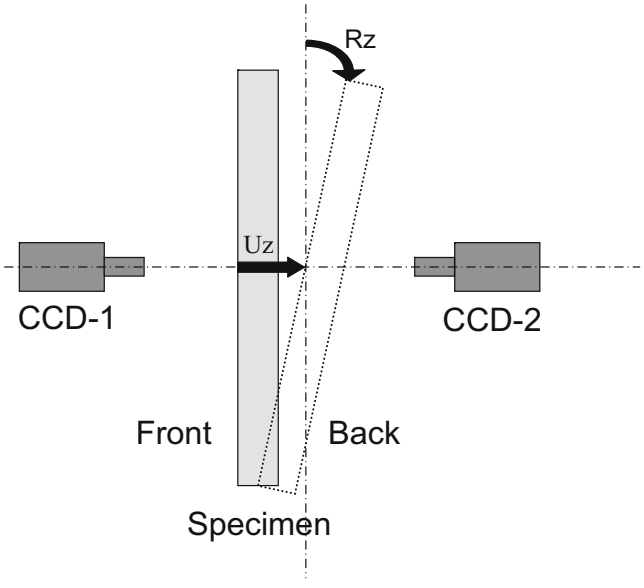

Fig. 4. Principle of the 2 cameras set-up

$$\varepsilon_x^{\text{front}} = \varepsilon_x^0 - \frac{M_y}{E_{xx} I_z} \frac{h}{2} \tag{10}$$

$$\varepsilon_x^{\text{back}} = \varepsilon_x^0 + \frac{M_y}{E_{xx} I_z} \frac{h}{2} \tag{11}$$

However, because of Eqs. 10 and 11, averaging strain maps over the two faces of the specimen will remove the bending contribution and give the actual in-plane strain ε_x^0 which is the strain ε_x to be measured:

$$\varepsilon_x = \varepsilon_x^0 = \frac{\varepsilon_x^{\text{front}} + \varepsilon_x^{\text{back}}}{2} \tag{12}$$

In practice, the grids on the two sides of the specimen are the same and the images on each face are taken at the same moment during loading. A reference mark on the side of the specimen is needed to match the back-to-back images for the calculation of the average displacements. The distance from each CCD camera and the specimen is checked in order to obtain the same magnification of the grid for the two images. The objective lens of the camera is set in order to sample one period with N pixels of the CCD sensor. During the setting up, N-1 out of the N pixels sampling a period are hidden in the recorded image of the grid. In this case, low-frequency fringes appear, resulting from a moiré effect [29]. The aim is to reduce the frequency of the fringes as much as possible. Once this task is completed, the setting of the camera lens is accurate enough to ensure reliable magnification and also phase computation. The uncertainty on the magnification is thus estimated at 2.6%.

The main conclusion of this section is that averaging out the strains over the two faces eliminates parasitic out-of-plane effects coming from both the change of magnification arising from out-of-plane displacements and bending deformation of the tested specimen.

Full-Field Measurements Results

The plane dog–bone specimen has been loaded up to 9,710 N, which corresponds to an average longitudinal stress of 243 MPa in the middle cross section of the specimen. The displacement rate was 0.05 mm/min. Pictures of the bonded grid have been grabbed all along

the loading process for time steps t_j separated by a constant time increment of 30 s.

Displacement Fields

According to the principle described before, displacement fields have been derived from the grid images grabbed at each load step on each side of the specimen. The following procedure has been applied:

- The displacement increment is computed from one load step to another, on each side of the specimen. As phase variations at any pixel are evaluated in the [-180°,180°] range, the loading increment between

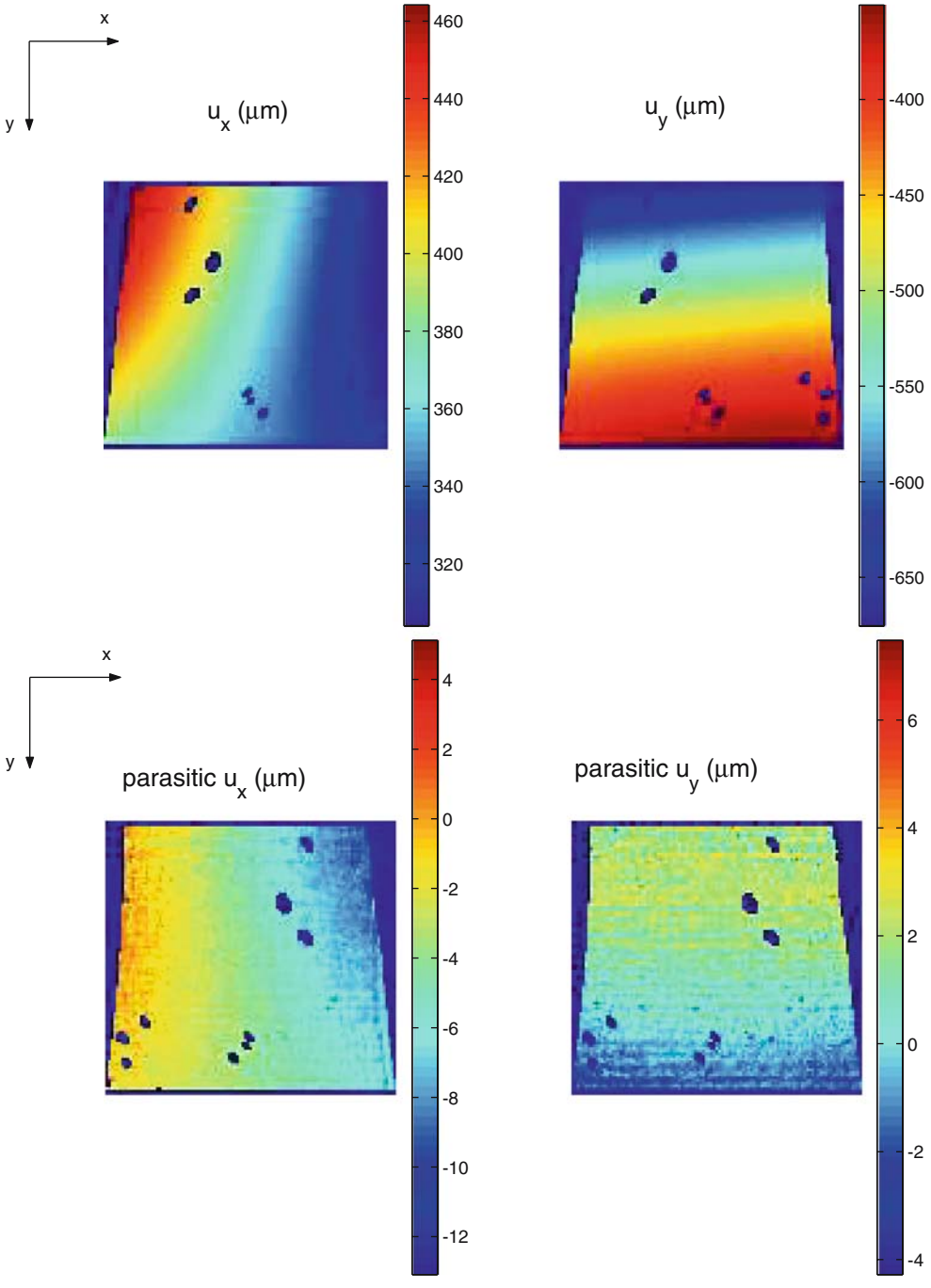

Fig. 5. In-plane raw displacement fields and parasitic displacement fields induced by out-of-plane motions and bending effects for 8,950 N (average stress of 224 MPa in the middle cross section) over the front face of the specimen

two consecutive load steps must be such that the increment of the whole displacement field remains in the range $[-p/2,p/2]$, where p is the pitch of the grid. This requirement has been fulfilled so as to avoid spatial phase unwrapping;

- The total displacement is computed on each side of the specimen by adding up the consecutive displacement increments;
- The displacement fields measured at each load step on the back face of the specimen is reversed and translated so that all the pixels have the same coordinates as their counterpart on the front face image;
- The in-plane displacement fields are computed at each load step as the average of the measured front face displacement field and the transformed back face displacement field (Fig. 5);

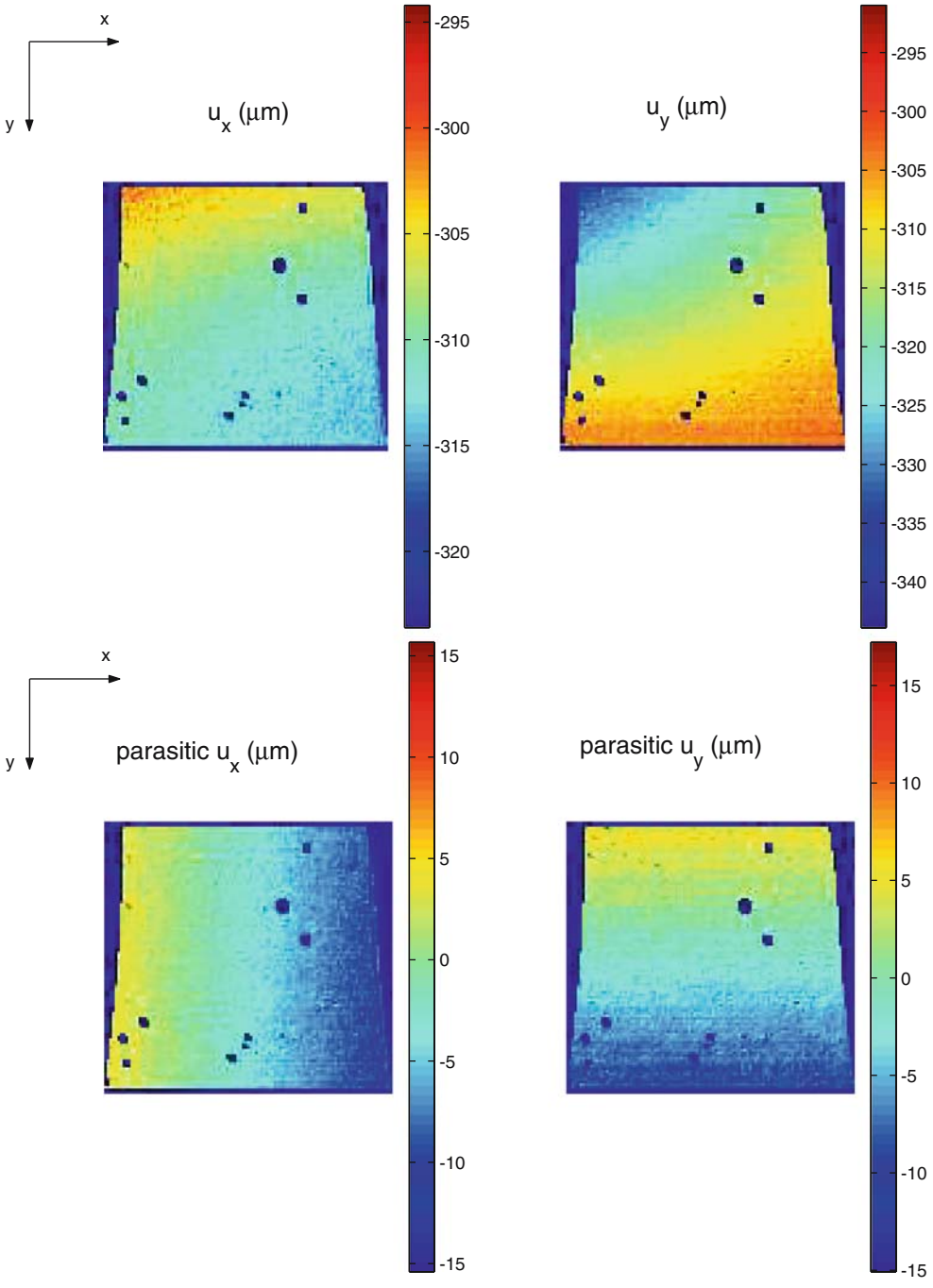

Fig. 6. In-plane raw displacement fields and parasitic displacement fields induced by out-of-plane motions and bending effects for the load corresponding to the onset of yielding

- The effect of averaging both sides measurements is visible by plotting the difference between the computed in-plane displacements on the front face and the raw measurements (example shown in Fig. 5 for a load of 8,950 N). The remaining displacements are only induced by out-of-plane motions and bending effects. They are negligible here compared to the in-plane displacements but they affect the measurements in a much more dramatic way for small loads, as can be seen on Fig. 6 where the induced parasitic strain $\varepsilon^{\text{parasitic}}$ derived from $u_x^{\text{parasitic}}$ and $u_y^{\text{parasitic}}$ is more than 5×10^{-4}, which is comparable to the actual in-plane strains.

Differentiation of the Displacement Fields

Obtaining the partial derivatives of the displacement field to calculate the strain field is a very critical aspect of the identification procedure. Indeed, this process amplifies the effect of noise and some filtering is necessary. Two main routes can be followed to tackle this problem:

- Convolution of the image with a gaussian kernel. This technique works all the better when the noise is spatially uncorrelated. However, when the noise is correlated over a number of pixels, this operation tends to spread it over a larger area. Moreover, the convolution is difficult to perform on the edges of the image;
- Provided that the displacement field is smooth enough (i.e., its spatial content is of much lower frequency than the noise), another powerful approach is polynomial fitting of the displacement field and analytic differentiation of the polynomials. Apart from very good high frequency noise filtering, the other nice features of this method are the interpolation of the missing data (grid defects) and the good tackling of the edges. A good way of choosing the order of the polynomial and checking the validity of the procedure is to plot the difference of the raw and fitted data. The result should be a random spatially uncorrelated signal if the fitting is appropriate.

Looking at the raw displacement fields (Fig. 5), it can be noticed that data are missing at several locations over the field area. These locations correspond to grid defects where the bonding procedure described in "Grid Bonding" failed. This problem of missing data is crucial for the differentiation and thus for the following identification. Accordingly, data interpolation is necessary and that is the reason why the polynomial fitting method has been chosen for processing the measured displacement fields. Two polynomials P_x and P_y are defined to approximate the displacement fields u_x and u_y:

$$\begin{cases} P_x(x,y) = \displaystyle\sum_{i=0}^{N}\sum_{j=0}^{N} a_{ij}\, x^i\, y^j \\ P_y(x,y) = \displaystyle\sum_{i=0}^{N}\sum_{j=0}^{N} b_{ij}\, x^i\, y^j \end{cases} \tag{13}$$

where N is the degree of the polynomials.

The coefficients a_{ij} and b_{ij} of polynomials are determined by minimizing the following quadratic deviation:

$$\begin{cases} R_x^2 = \dfrac{1}{pq}\left[\displaystyle\sum_{\mathrm{q}}\sum_{\mathrm{p}} w(x_p,y_q)\left[P_x(x_p,y_q)-u_x(x_p,y_q)\right]^2 - \left(\sum_{\mathrm{q}}\sum_{\mathrm{p}} w(x_p,y_q)\left[P_x(x_p,y_q)-u_x(x_p,y_q)\right]\right)^2\right] \\ R_y^2 = \dfrac{1}{pq}\left[\displaystyle\sum_{\mathrm{q}}\sum_{\mathrm{p}} w(x_p,y_q)\left[P_y(x_p,y_q)-u_y(x_p,y_q)\right]^2 - \left(\sum_{\mathrm{q}}\sum_{\mathrm{p}} w(x_p,y_q)\left[P_y(x_p,y_q)-u_y(x_p,y_q)\right]\right)^2\right] \end{cases} \tag{14}$$

where (x_p, y_q) are the coordinates of pixel locations and $w(x, y)$ is a weighting function. There are pixels where the grid image is disturbed mainly because of bonding defects. At these pixels location, the measured displacement is not reliable, and the data there can be considered as outliers. The weighting function $w(x, y)$ is used to prevent the outliers from affecting the derivation of the polynomial coefficients. Outliers are tracked

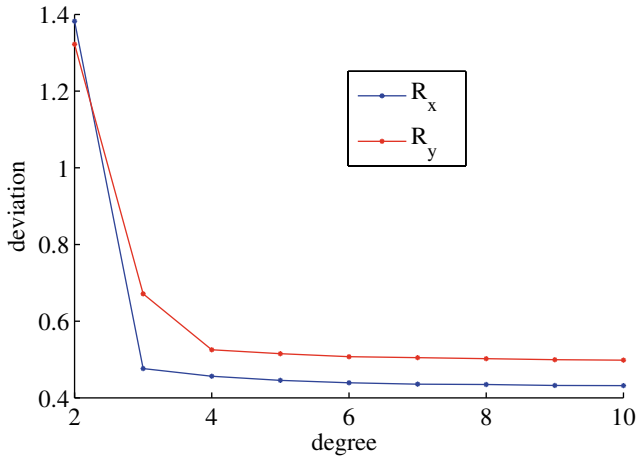

Fig. 7. Evolution of the R_x and R_y deviations with the degree of polynomials

by performing the algorithm a first time with $w(x, y)=1$ everywhere (except where data are missing) and then by detecting all the pixels where the difference between the polynomial and the raw data is superior to R_x or R_y.

The minimization is always achieved twice. The first time, the weighting function equals zero where data are missing and one everywhere else. After this first minimization, the differences $P_x(x_p, y_q) - u_x(x_p, y_q)$ and $P_y(x_p, y_q) - u_y(x_p, y_q)$ are computed at each pixel location and a zero weight is given for the next minimization to all the pixels where the difference is, respectively, superior to $2R_x$ and $2R_y$. Accordingly, eventual erroneous pixels are automatically removed.

R_x and R_y depend on the degree of the best polynomials approximating u_x and u_y (Fig. 7). When the degree increases, the R_x and R_y deviations decrease, tending to 0.5 μm, which is even lower than the displacement resolution $\sigma_u \simeq 0.95$ μm when averaging the data obtained on each face of the specimen (instead of 0.67 μm considering only one face) because possible erroneous pixels have been removed. R_x and R_y stay almost constant after degree 4. Thus, $N = 4$ has been chosen to process all the data in the following (Fig. 8).

It is difficult to assess the spatial resolution of this strain measurement. However, the fact that the remainders stay almost constant for polynomial degrees beyond four indicates that the spatial frequency of the mechanical phenomena occurring in the measured displacement fields has been reached. It can be verified by computing the distribution of the difference between the raw displacement field and the polynomial fits P_x and P_y (Fig. 9). Except for the presence of horizontal parasitic bands, the distribution looks similar to a white noise distribution and its amplitude is about 1% of that of the fitted fields.

The bands are probably induced by a defect of the grid itself. When investigating elastic solids with small deformations, those defects do not affect the measurement. They are automatically eliminated because they occur both in the initial and in the final phase fields and

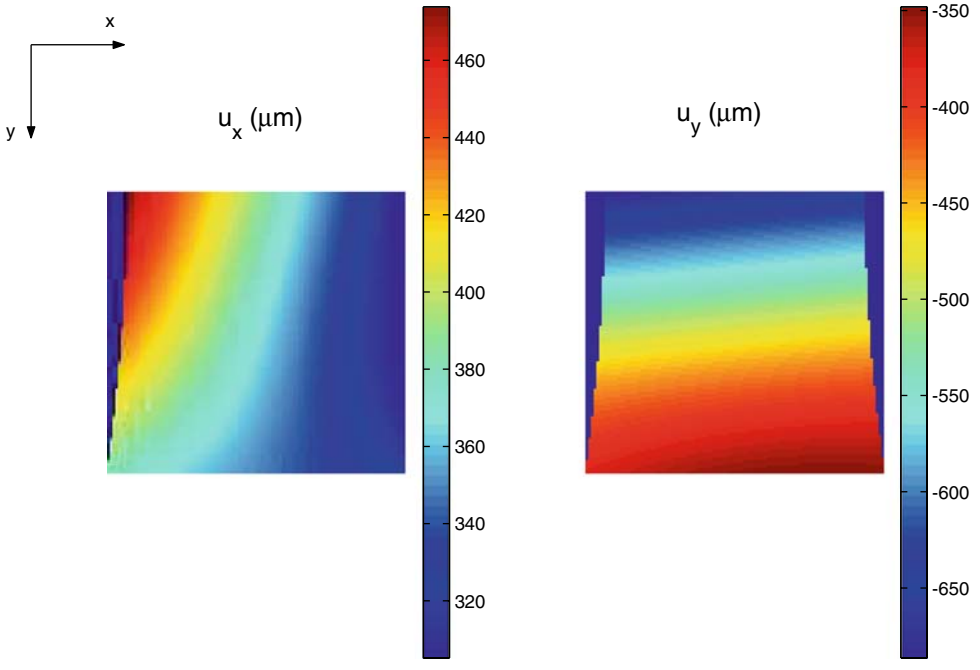

Fig. 8. Polynomially fitted displacement fields for 8,950 N (average stress of 224 MPa in the middle cross section)

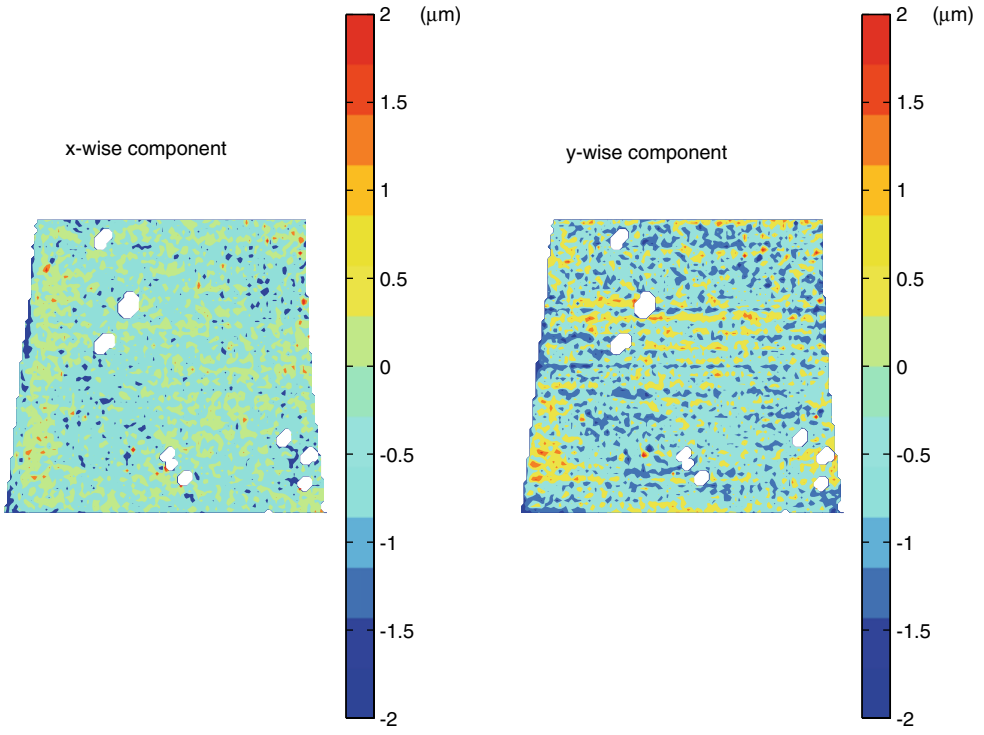

Fig. 9. Distribution of the difference between raw displacement field and polynomials P_x and P_y for 8,950 N (average stress of 224 MPa in the middle cross section)

approximately at the same location, so they are subtracted between each other when computing the displacement increments. Here, the vertical displacement is large because of the plastic behaviour of the material. It is more than three times the pitch of the grid for the 8,950 N load (Fig. 5). Therefore, the defects of the grid are not at the same location in the initial image and in the final image, inducing those parasitic stripes. Their presence is also a reason for using the polynomial fitting method because local differentiation would be strongly affected by it.

Finally, no deterministic mechanical phenomenon has been smoothed and hidden by the polynomial approximation. Only noise and measurement errors have been filtered (Fig. 9). This validates this approach for the current application.

Strain Results

An example of strain fields has been plotted for a load of 8,950 N (Fig. 10). They have been computed by analytical differentiation of the polynomials. The advantage is obviously that a very smooth strain distribution is obtained. This method would not be possible if a sharp strain concentration had existed somewhere over the field area. However, it has been proved just before that only noise and measurement errors have been filtered by the polynomial fitting approach in this application.

The effects induced by the dog-bone shape of the specimen onto the strain fields is the heterogeneity. Whereas straight specimen are supposed to provide a uniform distribution of strains and no shear, this test provides non zero shear strains and heterogeneous ε_{xx} and ε_{yy}. The following section will show how to identify accurately the constitutive parameters despite this unusual strain distribution.

Identification of the Elasto-Plastic Model

The Virtual Fields Method

The Virtual Fields Method (VFM) is based on the principle of virtual work [19]. This principle writes for static loading and in absence of volume forces:

$$-\int_V \underline{\underline{\sigma}} : \underline{\underline{\varepsilon}}^\star \mathrm{d}V + \int_{S_f} \vec{T}.\vec{u}^\star \mathrm{d}S = 0 \qquad (15)$$

where $\underline{\underline{\sigma}}$ is the actual stress tensor, $\underline{\underline{\varepsilon}}^\star$ is the virtual strain tensor, $\vec{T}$ is the distribution of applied loading acting on S_f, $\vec{u}^\star$ is the virtual displacement. An important feature is the fact that the above equation is verified for *any* kinematically admissible virtual field $(\vec{u}^\star, \underline{\underline{\varepsilon}}^\star)$. At this

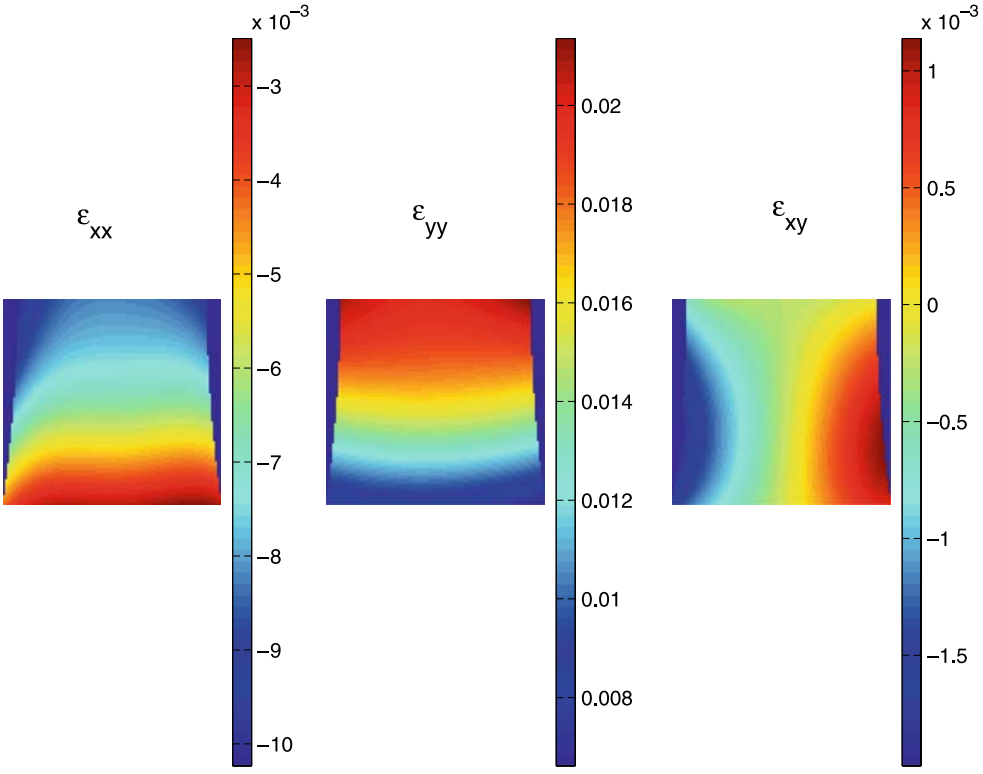

Fig. 10. Experimental strain fields for a load of 8,950 N (average stress of 224 MPa in the middle cross section)

stage, the constitutive equations are introduced. One can write in the general case:

$$\underline{\underline{\sigma}} = g(\underline{\underline{\varepsilon}}) \tag{16}$$

where g is a given function of the actual strain components but also of the constitutive parameters. Therefore, Eq. 15 writes in this case:

$$-\int_V g(\underline{\underline{\varepsilon}}) : \underline{\underline{\varepsilon}}^\star \mathrm{d}V + \int_{S_f} \vec{T}.\vec{u}^\star \mathrm{d}S = 0 \tag{17}$$

It is a trivial matter to see that any new virtual field in Eq. 17 leads to a new equation involving the constitutive parameters provided that the actual strain field is heterogeneous. The VFM relies on this important property. It is based on Eq. 17 written with a given set of virtual fields. This set of equations is used to extract the unknown constitutive parameters.

The choice of the virtual fields is a key issue in the method. Their number and their type depend on the nature of g in Eq. 16. Two cases must be distinguished:

- The constitutive equations depend linearly on the constitutive parameters (as in linear elasticity). In this case, writing Eq. 17 with as many virtual fields as unknowns leads to a linear system which directly provides the parameters after inversion, if that the actual strain field is heterogeneous and the virtual fields are independent [22, 23]. This will be illustrated in "Identification of the Elastic Parameters"
- The constitutive equations are not linear functions of the constitutive parameters. This case occurs for elasto-plasticity for instance. The identification strategy relies in this case on the minimization of a residual constructed with Eq. 17, as illustrated in "Identification of Plastic Parameters".

Identification of the Elastic Parameters

Before the occurrence of plastic strains, the response of the specimen is linear elastic. It is assumed that the specimen is in a state of plane stress. Accordingly, the relationship between stresses and strains writes for an isotropic material:

$$\begin{pmatrix} \sigma_{xx} \\ \sigma_{yy} \\ \sigma_{xy} \end{pmatrix} = \begin{bmatrix} \frac{E}{1-\nu^2} & \frac{\nu E}{1-\nu^2} & 0 \\ \frac{\nu E}{1-\nu^2} & \frac{E}{1-\nu^2} & 0 \\ 0 & 0 & \frac{E}{1+\nu} \end{bmatrix} \begin{pmatrix} \varepsilon_{xx} \\ \varepsilon_{yy} \\ \varepsilon_{xy} \end{pmatrix} \tag{18}$$

where E is Young's modulus and ν, Poisson's ratio.

Feeding Eq. 18 into Eq. 15, one gets:

$$\frac{E}{1-\nu^2}\int_S(\varepsilon_{yy}\varepsilon^\star_{yy}+\varepsilon_{xx}\varepsilon^\star_{xx})\mathrm{d}S+\frac{\nu E}{1-\nu^2}\times\int_S(\varepsilon_{xx}\varepsilon^\star_{yy}+\varepsilon_{yy}\varepsilon^\star_{xx})\mathrm{d}S+\frac{E}{1+\nu}\times\int_S\varepsilon_{xy}\varepsilon^\star_{xy}\mathrm{d}S=\frac{1}{t}\times\int_{S_f}\vec{T}.\vec{u}^\star\mathrm{d}S \quad (19)$$

where t is the thickness of the specimen and S is the area of the zone of interest (in black on Fig. 1).

Two virtual displacement fields have been considered. The first one denoted $\vec{v}^{\star 1}$ is such that:

- Below the region of interest ($y<0$), $v_x^{\star 1}(x,y)=v_y^{\star 1}(x,y)=0$
- In the region of interest ($0<y<L$), $v_x^{\star 1}(x,y)=0$ and $v_y^{\star 1}(x,y)=-y$
- Above the region of interest ($y>L$), $v_x^{\star 1}(x,y)=0$ and $v_y^{\star 1}(x,y)=-L$ where L is the length of the region of interest.

The second one denoted $\vec{v}^{\star 2}$ is such that:

- Below the region of interest ($y<0$), $v_x^{\star 2}(x,y)=v_y^{\star 2}(x,y)=0$
- In the region of interest ($0<y<L$), $v_x^{\star 2}(x,y)=x\,y\,(y-L)$ and $v_y^{\star 2}(x,y)=0$
- Above the region of interest ($y>L$), $v_x^{\star 2}(x,y)=0$ and $v_y^{\star 2}(x,y)=0$

Applying Eq. 19 with both virtual fields, one gets the following system:

$$\begin{cases}\dfrac{E}{1-\nu^2}\displaystyle\int_S\varepsilon_{yy}\mathrm{d}S+\dfrac{\nu E}{1-\nu^2}\int_S\varepsilon_{xx}\mathrm{d}S=\dfrac{PL}{t}\\[2ex]\dfrac{E}{1-\nu^2}\left[\displaystyle\int_S y(y-L)\varepsilon_{xx}\mathrm{d}S+\int_S x(2y-L)\varepsilon_{xy}\mathrm{d}S\right]+\\[2ex]\dfrac{\nu E}{1-\nu^2}\left[\displaystyle\int_S y(y-L)\varepsilon_{yy}\mathrm{d}S-\int_S x(2y-L)\varepsilon_{xy}\mathrm{d}S\right]=0\end{cases} \quad (20)$$

giving:

$$\begin{cases}\nu=-\dfrac{\int_S y\,(y-L)\,\varepsilon_{xx}\mathrm{d}S+\int_S x(2y-L)\varepsilon_{xy}\mathrm{d}S}{\int_S y\,(y-L)\,\varepsilon_{yy}\mathrm{d}S-\int_S x(2y-L)\varepsilon_{xy}\mathrm{d}S}\\[2ex]E=\dfrac{(1-\nu^2)\,PL}{t\left(\int_S\varepsilon_{yy}\mathrm{d}S+\nu\int_S\varepsilon_{xx}\mathrm{d}S\right)}\end{cases} \quad (21)$$

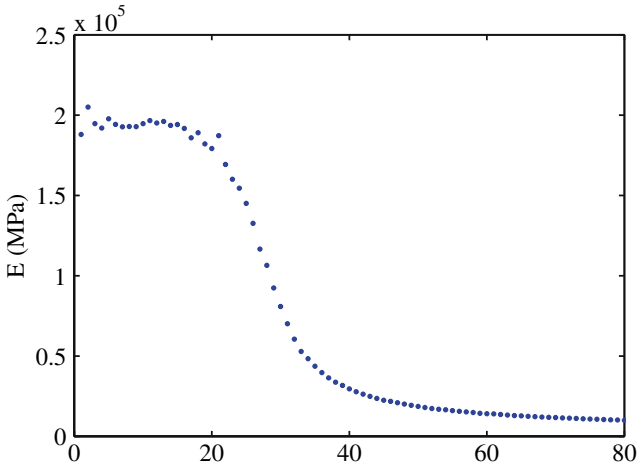

Fig. 11. Evolution of Young's modulus identified with the VFM at all applied loads

Equation 21 has been applied to the strain fields measured for all the load steps from 0 N up to 9,710 N (80 strain fields). The identified Young's modulus decreases drastically beyond the 16th load step (Fig. 11). It means that the yield stress has been reached and the behaviour is not linear elastic anymore.

Therefore, only the first 16 strain fields have been used to identify E and ν. The average of all the values are E = 205 GPa and ν = 0.29. Those values are very close to the values identified using standard tensile tests.

Identification of Plastic Parameters

Beyond the occurrence of plastic strains (16th load step according to Fig. 11), the relationship between stresses and strains is not linear anymore, at least over some pixels of the field area. For applying the VFM, one has to:

- Choose an initial guess of the unknown parameters;
- Use those parameters to compute the stress fields from the total strain fields measured with the grid method;
- Iterate until the derived stress fields verify at best the principle of virtual work.

Computation of the stresses from the measured strains

Deducing the stress field from the measured total strain field and an initial guess of the unknown parameters requires an adequate procedure. Procedures suited for a state of plane stress can be found in [37] or [25].

A highly simplified version of those procedures has been used here since the stress field is assumed to be uniaxial ($\sigma_{xx} = \sigma_{xy} = 0$), so the equivalent Von Mises stress reduces to $\sigma = \sigma_{yy}$ and the effective plastic strain writes: $\varepsilon^p = \varepsilon^p_{yy}$.

Let us consider a single pixel, denoted M. The measured longitudinal strain at pixel M and time t is denoted $\varepsilon_{yy}(t)$. The longitudinal stress at pixel M and time t is denoted $\sigma(t)$. The yield stress at pixel M and time t is denoted $Y(t)$. It is assumed that $Y(t_{15}) = \sigma_0$ and $\varepsilon^p(t_{15}) = 0$. Each load step j corresponds to the time denoted t_j.

Young's modulus E has already been identified using the strain maps before the 16th load step. For a given set of the constitutive parameters σ_0, R_0, R_{inf} and b, the procedure for computing the stress $\sigma(t_{j+1})$ can be sorted in three cases.

- Case 1: if $E[\varepsilon_{yy}(t_j) - \varepsilon^p(t_j)] \leq Y(t_j)$ and $E[\varepsilon_{yy}(t_{j+1}) - \varepsilon^p(t_j)] \leq Y(t_j)$, then the deformation is purely elastic between load step j and load step $j+1$ at pixel M:

$$\begin{cases} \sigma(t_{j+1}) = E[\varepsilon_{yy}(t_{j+1}) - \varepsilon^p(t_j)] \\ \varepsilon^p(t_{j+1}) = \varepsilon^p(t_j) \\ Y(t_{j+1}) = Y(t_j) \end{cases} \tag{22}$$

- Case 2: if $E\,\varepsilon_{yy}(t_j) = Y(t_j)$ and $E\,\varepsilon_{yy}(t_{j+1}) > Y(t_j)$, then the deformation is elasto–plastic between load step j and load step $j+1$ at pixel M.
The effective plastic strain $\varepsilon^p(t_j)$ and stress $\sigma(t_j)$ are assumed to be known from the computations at the previous load step. This is only possible if case 2 does not occur for the first load step which is considered. In order to fulfil this requirement, the first stress field is computed for the 16th load step.
Accordingly, a differential equation has to be solved for computing the increment of ε^p from $\varepsilon_{yy}(t_j)$ and $\varepsilon_{yy}(t_{j+1})$ [37, 38]. It writes:

$$\frac{\partial \varepsilon^p}{\partial t} = \frac{E\dfrac{\partial \varepsilon_{yy}}{\partial t}}{\left(E + \dfrac{\partial \sigma}{\partial \varepsilon^p}\right)} = \frac{E\left[\varepsilon_{yy}(t_{j+1}) - \varepsilon_{yy}(t_j)\right]/(t_{j+1} - t_j)}{E + R_0 + b\ R_{\text{inf}} \exp(-b\,\varepsilon^p)} \tag{23}$$

The differential equation is solved using the Euler numerical method. The time increment between the two strain field measurements at step j and step $j+1$ has been divided in N substeps j_k and the effective plastic strain $\varepsilon^p(t_{j_k})$ has been computed substep by substep between the measured strain field $\varepsilon_{yy}(t_j)$ and the measured strain field $\varepsilon_{yy}(t_{j+1})$ according to:

$$\begin{cases} \varepsilon^p(t_{j_{k+1}}) = \varepsilon^p(t_{j_k}) + \dfrac{E\left[\varepsilon_{yy}(t_{j+1}) - \varepsilon_{yy}(t_j)\right]/N}{E + R_0 + b\,R_{\text{inf}} \exp\left[-b\ \varepsilon^p(t_k)\right]} \\ \varepsilon^p(t_{j_0}) = \varepsilon^p(t_j) \end{cases} \tag{24}$$

N has been chosen so that the total strain increment between two substeps is lower than 10^{-4} at the knee point of the stress–strain curve and lower than 10^{-3} for the asymptotic part. For that reason, N is different from one pixel M to another (see flowchart in Fig. 12). This particular choice for N ensures the convergence of the Euler numerical method in this application. Finally, the unknown quantities at load step $j+1$ are:

$$\begin{cases} \sigma(t_{j+1}) = E\left[\varepsilon_{yy}(t_{j+1}) - \varepsilon^p(t_{j_N})\right] \\ \varepsilon^p(t_{j+1}) = \varepsilon^p(t_{j_N}) \\ Y(t_{j+1}) = \sigma_0 + R_0\varepsilon^p(t_{j_N}) + R_{\text{inf}}\left\{1 - \exp\left[-b\,\varepsilon^p(t_{j_N})\right]\right\} \end{cases} \tag{25}$$

- Case 3: if $E\,[\varepsilon_{yy}(t_j) - \varepsilon^p(t_j)] \leq Y(t_j)$ and $E\,[\varepsilon_{yy}(t_{j+1}) - \varepsilon^p(t_j)] > Y(t_j)$, then there is a transition from an elastic to an elasto–plastic deformation between load step j and load step $j+1$ at pixel M. The algorithm of case 2 is applied with $\varepsilon_{yy}(t_{j_0}) = Y(t_j)/E$ and $\varepsilon^p(t_{j_0}) = \varepsilon^p(t_j)$.

Minimization of the deviation from the principle of virtual work

The identification procedure relies on the fact that the stresses calculated using the above procedure must be statically admissible (ie, they must respect the equilibrium equations). This is checked using the principle of virtual work applied with n independent virtual fields (see below). A cost function is therefore built up as:

$$\mathcal{C}(\sigma_0, R_0, R_{\text{inf}}, b) = \sum_{i=1}^{n} \sum_{j=16}^{80} \left[-\int_V \underline{\underline{\sigma}}(t_j) : \underline{\underline{\varepsilon}}^{\star i}\, \mathrm{d}V + \int_S \vec{T}(t_j).\vec{u}^{\star i}\, \mathrm{d}S \right]^2 \tag{26}$$

where $\vec{u}^{\star i}$ is a kinematically admissible virtual field and $\underline{\underline{\varepsilon}}^{\star i}$ are the virtual strain fields derived from $\vec{u}^{\star i}$; $\underline{\underline{\sigma}}(t_j)$ is

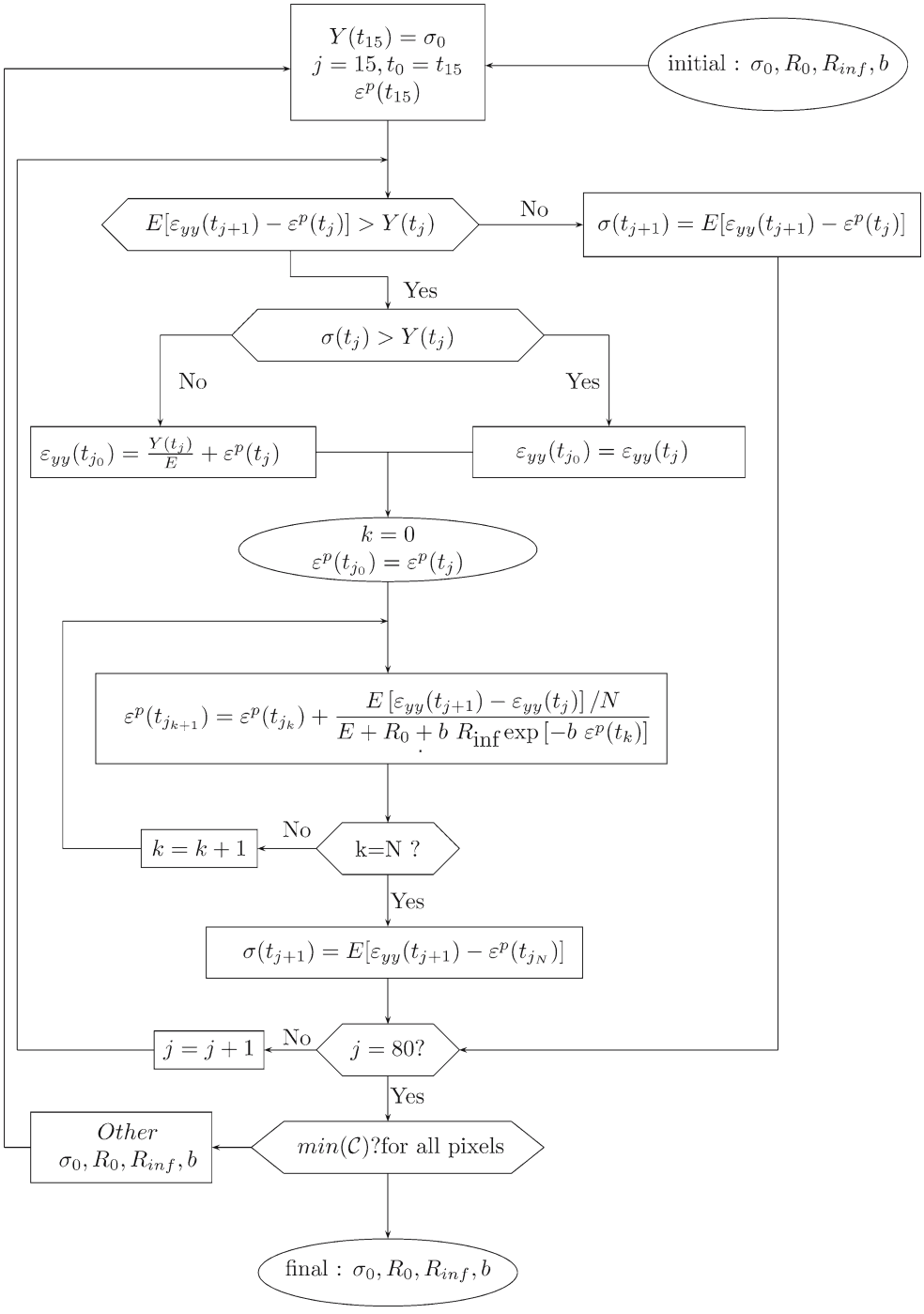

Fig. 12. General flowchart of the numerical procedure for computing stress fields from experimental in–plane strain fields

the actual stress field at time t_j computed as explained in the previous section with set of assumed parameters σ_0, R_0, R_{inf} and b. The stress field is computed at 65 different time steps, which correspond to the 65 displacement fields available beyond the occurrence of plasticity (the first occurrence of plasticity is detected at load step 16 and the last load step when the test has been stopped is load step 80).

The virtual fields $\vec{u}^{\star i}$ chosen here are defined as $\vec{v}^{\star 1}$ in "Identification of the Elastic Parameters", but over a smaller length located between abscissa y_i and y_{i+1} such that:

- For $y > y_{i+1}$, $u_x^{\star i}(x, y) = u_y^{\star i}(x, y) = 0$
- For $y_i < y < y_{i+1}$, $u_x^{\star i}(x, y) = 0$ and $u_y^{\star i}(x, y) = -y$
- For $y < y_i$, $u_x^{\star i}(x, y) = 0$ and $u_y^{\star i}(x, y) = y_i - y_{i+1}$

Table 2 Comparison of the identified Voce's model parameters with reference values and cost function sensitivities, $n = 100$, d = 4, convergence after 334 iterations

Parameter	Reference value (Mean $\pm 2\sigma$)	Initial value	Identified value with the VFM	Cost function sensitivity
$E(GPa)$	199±5.17	-	195	
ν	0.32±0.02	-	0.20	
$\sigma_0(MPa)$	127±15	100	140	300
$R_0(GPa)$	2.46±0.49	0.2	2.19	16
$R_{\text{inf}}(MPa)$	56.2±13.8	100	46.4	50
b	3.37±0.72 $\times 10^3$	100	2.46×10^3	1.3

The area of interest of the specimen has been divided in n elements of equal length $y_{i+1} - y_i = L/n$ and of area S_i. Therefore, the cost function of Eq. 26 becomes:

$$\mathcal{C}(\sigma_0, R_0, R_{\text{inf}}, b) = \sum_{i}^{n} \sum_{j=16}^{80} \left[\frac{\frac{P(t_j)L}{tn} - \int_{S_i} \sigma(t_j) \mathrm{d}S}{\frac{P(t_j)}{tw} S_i} \right]^2 \tag{27}$$

The denominator $\frac{P(t_j)}{ew} S_i$ has been introduced in order to provide dimensionless quantities where the weight of each term is the same whatever the applied load or the observed cross section; w is the width of the cross section located at the middle of the region of interest and t is the thickness of the specimen.

A minimization has been performed to find the minimum of the cost function $\mathcal{C}(\sigma_0, R_0, R_{\text{inf}}, b)$, using a Nelder Mead algorithm available in the Matlab software within the *fminsearch* command.

Identification Results and Discussion

First results

The first set of results has been obtained with the following parameters:

- 4th order polynomial for fitting the displacements and deriving the strains (d = 4);
- $n = 100$ for the cost function of Eq. 27;
- Starting point for the optimization: $\sigma_0^i = 100\ MPa$, $R_0^i = 200\ MPa$, $R_{\text{inf}}^i = 100\ MPa$ and $b^i = 100$.

The convergence criterion was that both the cost function and the parameters should not move by more than 0.1 between two consecutive iterations. The results of the identification are reported in Table 2. The first information is that Young's modulus is very well identified, although at the beginning of the test, the strain field is significantly influenced by parasitic in-plane bending (non symmetric strain maps with respect to y). However, Poisson's ratio is underestimated here mainly because the strain values involved are reaching the strain sensitivity of the measurement technique (a few 10^{-4}). For the plastic parameters, it can be seen that all parameters are identified within the $\pm 2\sigma$ bounds of the reference, except b. In order to investigate this point, the sensitivities of the cost function to each parameter has been calculated. To do so, for each parameter, the three others are fixed to the reference and the evolution of the cost function is calculated with respect to the fourth one, around the reference value. Then, a second order polynomial is fitted through these data and the second derivative is taken. This sensitivity is therefore the curvature of the cost function along the direction of the considered parameter. It can be seen that the best identified parameter is σ_0 (initial yield stress). Then, R_{inf}, which is the intersection of the asymptotic line with the stress axis and R_0, the slope of the asymptotic line. The parameter characterizing the curvature of the non linear transition zone, b, is not so well identified, with the sensitivity to b being the lowest, thus giving a possible explanation for the difference on b between the full-field identification and the reference.

Another possible explanation for the shift in b could be the effect of the triaxiality of the stress field since

Table 3 Comparison of the identified Voce's model parameters with the VFM from FE simulated data with reference values used to generate the FE data

Parameter	Reference value	VFM identified value	Relative difference (%)
σ_0	127 MPa	130 MPa	-2.4
R_0	2.46 GPa	2.44 GPa	0.8
R_{inf}	56.2 MPa	54.9 MPa	2.2
b	3.37×10^3	3.39×10^3	-0.7

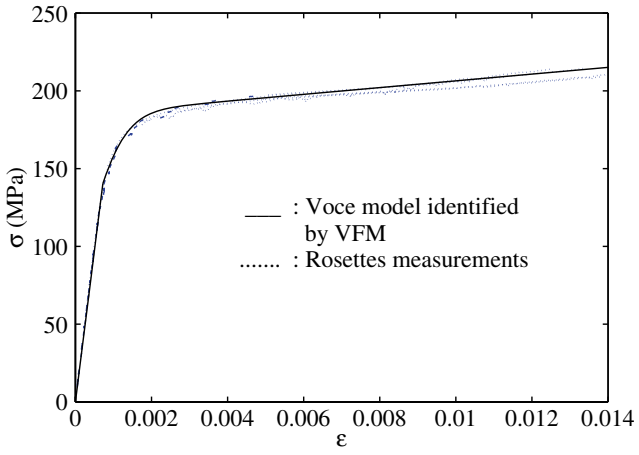

Fig. 13. Superposition of the identified Voce's law and rosettes measurements from the VFM

the analysis here is uniaxial. In order to check this assumption, the above optimization has been performed with finite element simulated data (from the simulation presented in "Heterogeneous Mechanical Test"). The results are presented in Table 3. It can be seen that the hypothesis of uniaxiality of the stress state does not disturb the identification very significantly. Therefore, this is not the right track to explain the difference on b reported in Table 2.

The VFM identified response has been plotted together with the stress-strain curves from the strain gauges measurements (reference) on Fig. 13. This plot clearly shows that the identification is very satisfactory except in the transition bend to the linear hardening, which is exactly the part driven by b. In order to check that this problem does not arise because of the model itself, the fit with the reference parameters is plotted together with the raw data from the strain gauges on Fig. 14. It can be seen that the same effect appears, just less acutely. Therefore, the difference observed in Fig. 13 comes both from the model and the error on b. One possibility for this error could also be the fact that the reference test only processes the onset of plasticity as an average as the present procedure takes into account all the points of the active area and is therefore more rigourous (no assumption on the distribution of the σ_{yy} stress component here). The term 'reference' for the data from the uniform test should therefore be considered with care.

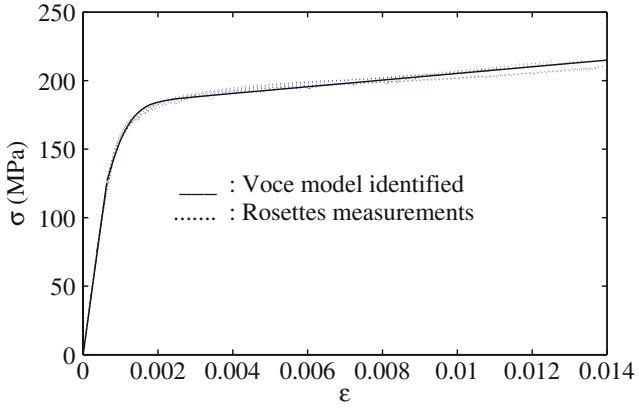

Fig. 14. Superposition of the identified Voce's law and rosettes measurements from least-square fit (reference)

As always in such inverse procedures, there are a number of numerical parameters involved that have to be chosen a *priori* before launching the optimization. The objective of the following paragraphs is to investigate the effects of some of these parameters on the identified values in order to gain confidence in the results.

Influence of the initial values

It is well-known in optimization that the initial values chosen to initiate the process have a great influence on the results, particularly if the cost function has many local minima. In order to get a feel for this, the above process has been launched with three other starting points, as reported in Table 4. Each time, the converged values of the four plastic parameters were the same (less than 0.1% difference). Just the number of iterations varied depending on the distance between initial and final values. This is very reassuring as to the smoothness of the cost function. It should however be stated that if initial values are taken unrealistically, then convergence can lead to different values, so that the smoothness quality of the cost function only extend over a certain distance around the reference (represented by the domain covered by the different trial values of Table 4). In particular, a local minimum was consistently found at $\sigma_0 = 170$ MPa, $R_0 = -700$ MPa, $R_{\text{inf}} = 90$ MPa and $b = 60$, with a value for the cost function about five times higher than that at the correct minimum. The negative hardening modulus R_0 is

Table 4 Convergence iterations for different sets of trial values

Parameter	Identified (VFM)	Set 1	Set 2	Set 3	Set 4
$\sigma_0(MPa)$	140	100	1,000	40	1,000
$R_0(GPa)$	2.19	0.2	0.1	0.01	1
$R_{\text{inf}}(MPa)$	46.4	100	1000	10	100
b	2,460	100	10,000	10,000	1,000
Nb iter.	-	334	800	640	369

Table 5 Influence of the virtual fields (n: number of sections considered)

Parameter	n=1	n=2	n=4	n=10	n=25	n=50	n=100
$\sigma_0(MPa)$	138	140	141	140	140	140	140
$R_0(MPa)$	2,230	2,197	2,194	2,194	2,195	2,195	2,195
$R_{\text{inf}}(MPa)$	48.2	46.4	45.9	46.2	46.4	46.4	46.4
b	2,803	2,519	2,445	2,546	2,464	2,465	2,465

clearly unrealistic here and this local minimum could easily be avoided by using constrained optimization (all values positive, for instance).

Influence of the virtual field

Another important parameter for the process is the choice of the cost function, i.e.,, the choice of the virtual fields. In order to test this influence, different values for n have been considered, from 1 (uniform virtual strain field over the whole specimen) to $n = 100$ (piecewise virtual fields considering each time only one row of pixels). Table 5 reports the results, using the first set of trial values (Table 2). It is clear that except for $n = 1$, all the other results are very close, indicating a limited effect of the choice of the virtual field. This is here certainly because of the rather simple stress and strain field. It should be also pointed out that if the other starting points are used (see Table 4), the results are the same except for trial set 2 for certain values of n where the local minimum described previously is reached.

Influence of the fitting polynomial degree

The final set of results concern the influence of the degree of the polynomial used to fit the displacement data and derive the strains. The results are reported in Table 6 for $n = 100$ and the first set of initial values. It appears that the results are more sensitive to this parameter. However, even for degree 2 which is clearly a very rough approximation (see Fig. 7), the results are close to the reference. The sensitivity of the identified values to the polynomial degree can be summarized by the coefficient of variation (standard deviation/average in %) in Table 6. It is interesting to note that these coefficients are rather low (compared to that of the reference values in Table 2, even for b, which however is confirmed to be the less sensitive parameter in this configuration.

Conclusion

The present study has shown that it is possible to identify elasto-plastic parameters from a heterogeneous test, full-field displacement measurements with the grid method and inverse identification with the virtual fields method. The quality of the present results are clearly linked to the careful full-field measurements and in particular, the two-cameras set up. Moreover, variations of some of the parameters involved in the process (degree of fitting polynomial, trial values, virtual fields) have shown good stability of the identified values, giving confidence in the present results. It must be underlined again that to the knowledge of the authors, this is the very first experimental validation of the virtual fields method in the case of elasto-plastic materials and it opens the way to a very large and promising area of experimental mechanics in the future.

The approach is obviously to be improved. Computing all the components of the stress tensor from experimental strain fields and involving them with more sophisticated virtual fields would probably provide more accurate results. Further work will also be aimed at using a more complex test geometry (asymmetrically double-notched specimen) to validate the approach for fully multidirectional stress states. Then, applications to large strain (forming processes), high strain rate testing, heterogeneous materials (welds) or identification at the microscale are very interesting future directions.

Table 6 Influence of the fitting polynomial degree on the identified parameters

	Degree 2	Degree 3	Degree 4	Degree 5	Degree 6	Degree 7	Moy.	C.V. (%)
σ_0 (MPa)	138	140	141	136	137	141	138, 5	1, 4
R_0 (GPa)	2, 18	2, 2	2, 19	2, 21	2, 19	2, 19	2, 19	0, 4
R_{inf} (MPa)	48, 3	47, 1	46, 3	50, 9	50	46, 2	48, 1	4, 1
b $(\times 10^3)$	3, 13	2, 75	2, 46	2, 75	2, 52	2, 24	2, 65	12

Acknowledgments The authors are grateful to the "Conseil Régional de Champagne Ardenne" for its financial support to this study and to Professor Michel Grédiac for a long standing collaboration on the virtual fields method and fruitful discussions related to the present paper.

References

1. Mahnken R, Stein E (1996) Parameter identification for viscoplastic models based on analytical derivatives of a least-squares functional and stability investigations. Int J Plast 12:451–476.
2. Mahnken R (1999) Aspects on the finite element implementation of the gurson model including parameter identification. Int J Plast 15:1111–1137.
3. Bruhns OT, Anding DK (1999) On the simultaneous estimation of model parameters used in constitutive laws for inelastic material behaviour. Int J Plast 15:1311–1340.
4. Harth T, Schwan S, Lehn J, Kollmann FG (2004) Identification of material parameters for inelastic constitutive models: statistical analysis and design of experiments. Int J Plast 20:1403–1440.
5. Yoshida F, Urabeb M, Hinoa R, Toropov VV (2004) Inverse approach to identification of material parameters of cyclic elasto-plasticity for component layers of a bimetallic sheet. Int J Plast 19:2149–2170.
6. Laws V (1981) Derivation of the tensile stress-strain curve from bending data. J Mater Sci 16:1299–1304.
7. Mayville RA, Finnie I (1982) Uniaxial stress-strain curves from a bending test. Exp Mech 22:197–201.
8. Brunet M, Morestin F, Godereaux S (2001) Nonlinear kinematic hardening identification for anisotropic sheet metals with bending-unbending tests. J Eng Mater Technol 123:378–383.
9. Zhao KM (2004) Inverse estimation of material properties for sheet metals. Commun Numer Methods Eng 20:105–118.
10. Kajberg J, Sundin KG, Melin LG, Ståhle P (2004) High strain rate tensile and viscoplastic parameter identification using micoscopic high-speed photography. Int J Plast 20:561–575.
11. Mahnken R, Stein E (1994) The identification of parameters for visco-plastic models via finite-elements methods and gradient methods. Model Simul Mater Sci Eng 2:597–616.
12. Mahnken R, Stein E (1996) A unified approach for parameter identification of inelastic material models in the frame of the finite element method. Comput Methods Appl Mech Eng 136:225–258.
13. Meuwissen MHH (1998) An inverse method for the echanical characterisation of metals. PhD thesis, Eindhoven Technical University, The Netherlands.
14. Meuwissen MHH, Oomens CWJ, Baaijens FPT, Petterson R, Janssen JD (1998) Determination of the elasto-plastic properties of aluminium using a mixed numerical-experimental method. J Mater Process Technol 75:204–211.
15. Okada H, Fukui Y, Kumazawa N (1999) An inverse analysis determining the elastic-plastic stress-strain relationship using nonlinear sensitivities. Comput Model Simul Eng 4(3):176–185.
16. Hoc T, Crépin J, Gélébart L, Zaoui A (2003) A procedure for identifying the plastic behaviour of single crystals from the local response of polycrystals. Acta Mater 51:5477–5488.
17. Kajberg J, Lindkvist G (2004) Characterization of materials subjected to large strains by inverse modelling based on in-plane displacement fields. Int J Solids Struct 41:3439–3459.
18. Geng L, Shen Y, Wagoner, RH (2002) Anisotropic hardening equations derived from reverse-bend testing. Int J Plast 18(5–6).
19. Grédiac M (1989) Principe des travaux virtuels et identification. Comptes Rendus de l'Académie des Sciences 309(2):1–5 (in French with English abstract).
20. Grediac M, Pierron F, Surrel Y (1999) Novel procedure for complete in-plane composite characterization using a single T-shaped specimen. Exp Mech 39(2):142–149.
21. Moulart R, Avril S, Pierron F (2006) Identification of the through-thickness rigidities of a thick laminated composite tube. Composites Part A: Applied Science and Manufacturing, Oregon.
22. Grediac M, Toussaint E, Pierron F (2002) Special virtual fields for the direct determination of material parameters with the virtual fields method. 1–Principle and definition. Int. J. Solids Strucs. 39(10):2691–2705.
23. Grediac M, Toussaint F, Pierron E (2002) Special virtual fields for the direct determination of material parameters with the virtual fields method. 2–application to in-plane properties. Int. J. Solids Strucs. 39(10):2707–2730.
24. Avril S, Gédiac M, Pierron F (2004) Sensitivity of the virtual fields method to noisy data. Comput. Mech. 34(6): 439–452.
25. Grediac M, Pierron F (2005) Applying the virtual field method to the identification of elasto-plastic constitutive parameters. Int J Plast. 26(4):602–607.
26. Voce E (1955) A practical strain-hardening function. Metallurgia 51:219–226.
27. Kobayashi A (1993) Handbook on Exp Mech, 2nd edn. Society for Exp Mech, Connecticut.
28. Surrel Y Optique C1. http://www.cnam.fr/instrumesure/.
29. Surrel Y (1994) Moiré and grid methods: a signal processing approach. In: Ryszard J. Pryputniewicz, Jacek Stupnicki (eds) Interferometry '94: photomechanics, vol. 2342. The International Society for Optical Engineering, pp. 213–220.
30. Creath K (1988) Phase measurement interferometry techniques. In: Wolf E (ed) Progress in optics, Elsevier, Amsterdam, The Netherlands; New York, vol. 26, chap. 5, pp. 349–383.
31. Phillion DW (1997) General methods for generating phase-shifting interferometry algorithms. Appl Opt 36(31):8098–8115.
32. Surrel Y (1996) Design of algorithms for phase measurements by the use of phase-stepping. Appl Opt 35(1):51–60.
33. Surrel Y (2000) Fringe analysis. In: Rastogi PK (ed) Photomechanics / TAP77. Springer, Berlin Heidelberg New York, pp. 57–104.
34. Parks VJ (1993) Geometric moiré. In: Kobayashi A (ed) Handbook on experimental mechanics, 2nd edn. Society for Exp Mech, Connecticut, chap. 6, pp. 267–296,
35. Post D (1982) Developments in moiré interferometry. Opt Eng 21(3):458–467.
36. Piro J-L, Grédiac M (2004) Producing and transferring low-spatial-frequency grids for measuring displacement fields with moiré and grid methods. Exp Tech 28(4):23–26.
37. Sutton MA, Deng X, Liu J, Yang L (1996) Determination of elastic-plastic stresses and strains from measured surface strain data. Exp Mech 36(2):99–112.
38. Lemaître J, Chaboche J-L (1990) Mechanics of solid materials. Cambridge University Press, UK.